

# Imaging of the solar atmosphere by the Siberian Solar Radio Telescope at 5.7 GHz with an enhanced dynamic range

Alexey KOCHANOV, Sergey ANFINOGENTOV, Dmitry PROSOVETSKY, George RUDENKO, Victor GRECHNEV  
*Institute of Solar-Terrestrial Physics SB RAS, Lermontov St. 126A, Irkutsk 664033, Russia*  
*anfinogentov@iszf.irk.ru, kochanov@iszf.irk.ru*

(Received ; accepted )

## Abstract

The Siberian Solar Radio Telescope (SSRT) is a solar-dedicated directly-imaging interferometer observing the Sun at 5.7 GHz. The SSRT operates in the two-dimensional mode since 1996. The imaging principle of the SSRT restricts its opportunities in observations of very bright flare sources, while it is possible to use ‘dirty’ images in studies of low-brightness features, which do not overlap with side lobes from bright sources. The interactive CLEAN technique routinely used for the SSRT data provides imaging of active regions but consumes much time and efforts and does not reveal low-brightness features below the CLEAN threshold. The newly developed technique combines the CLEAN routine with the directly-imaging capability of the SSRT and provides clean images with an enhanced dynamic range automatically. These elaborations considerably extend the range of tasks, which can be solved with the SSRT. We show some examples of the present opportunities of the SSRT and compare its data with the images produced by the Nobeyama Radioheliograph at 17 GHz as well as observations in different spectral ranges.

**Key words:** instrumentation: interferometers, techniques: image processing, Sun: radio radiation

## 1. Introduction

Microwaves provide extensive opportunities to study quiet and dynamic solar features from chromospheric to coronal heights by observing their thermal free-free and gyromagnetic emissions. The Siberian Solar Radio Telescope (SSRT; Smolkov et al. 1986; Grechnev et al. 2003) is a solar-dedicated interferometer observing the Sun in total intensity (Stokes  $I$ ) and circular polarization (Stokes  $V$ ) at a frequency of 5.7 GHz ( $\lambda = 5.2$  cm). The SSRT is a rather old instrument initially proposed in 1960-s and constructed in 1970–1980-s. Having started to observe in 1980-s in the one-dimensional mode, the SSRT underwent a number of upgrades of both the hardware and software systems. First two-dimensional maps were obtained in 1991 from one-dimensional SSRT observations by Alissandrakis et al. (1992) using the Earth-rotation aperture synthesis techniques. Fast one-dimensional imaging started in 1992 (Altyntsev et al. 1994). Regular production of several images per day in the two-dimensional mode commenced in 1996. The observations at the SSRT have been interrupted in July 2013 due to a fundamental upgrade.

The SSRT is located in Badary forest area 220 km from Irkutsk at N  $51^{\circ}45'$ , E  $102^{\circ}13'$ . The SSRT is a cross-shaped interferometer consisting of two equidistant linear arrays in the East–West and North–South directions, each of 128 antennas spaced by 4.9 m (Figure 1). Each linear interferometer has a baseline of 622.3 m. Unlike synthesizing interferometers such as the Nobeyama Radioheliograph (NoRH; Nakajima et al. 1994), the SSRT produces images directly without measuring visibilities. The imaging process invokes the solar rotation for the

scanning in the hour angle and the so-called ‘frequency scanning’ technique in the altitude (over 5.67–5.79 GHz). One full-disk solar image with a field of view of  $42' \times 42'$  is composed typically in 3 to 5 minutes. The SSRT produces several tens of single-pass images, depending on the Sun’s declination (i.e., season). The overall SSRT sensitivity in solar observations is about 1500 K for an image formed in a single pass of the Sun (integration time 0.336 s). The system noise contribution is about 800 K. The dynamic range of the raw data is about 30 dB.

The directly-imaging operating principle of the SSRT determines a relatively low level of the side lobes (22% of the main maximum for the non-distorted beam) and therefore allows one to use even ‘dirty’ maps occasionally, when radio sources on the Sun are not very bright (Uralov et al. 1998; Grechnev et al. 2003; 2006a). However, in a typical situation, contributions from the beam’s side lobes make the deconvolution of the SSRT images quite necessary.

The basic deconvolution algorithm in the solar radio astronomy is the CLEAN method proposed by Högbom (1974) due to its robustness, although successful examples are known of invoking different techniques such as MEM (e.g., Enome 1995; Nindos et al. 1999). CLEAN provides reliable results for compact features like gyromagnetic sources in solar active regions but is not well-suited for extended sources. The deconvolution of such sources using the classical CLEAN method results in the so-called ‘fringing’, i.e., dividing a single continuous object into a multitude of small bright features. These artifacts of the original CLEAN method make it less suitable for the deconvolution of extended solar features such as the ‘bald’ solar disk, filaments, coronal holes, etc. Nindos et

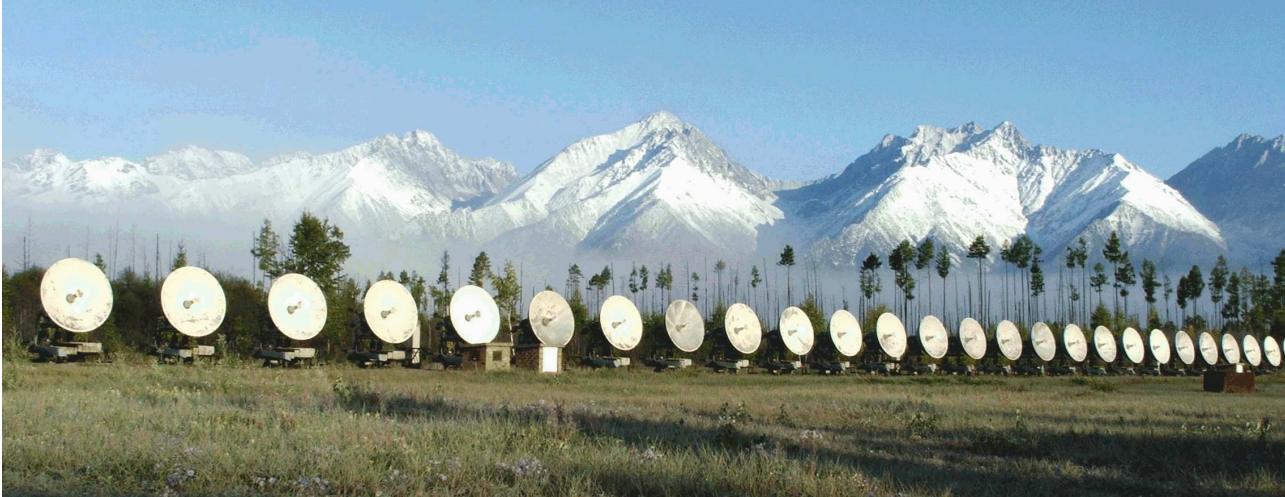


**Fig. 1.** View of the SSRT North arm.

al. (1999) showed that different deconvolution methods such as the Steer CLEAN (Steer et al. 1984) and even MEM also suffered from this problem.

The performance of the CLEAN algorithm for extended sources can be improved by adopting the multi-scale approach, in which the sources to be recovered are modeled as being composed of various different scale sizes. The deconvolution technique routinely used at the SSRT up to the recent time was, in fact, one of the first implementations of this approach (Lesovoy 2002). This technique successfully deconvolved bright sources in active regions, but did not recover low-brightness features, thus decreasing the dynamic range of the clean maps to about 20 dB. This circumstance is consistent with the conclusion drawn by Koshiishi et al. (1994) for NoRH that the final image quality is not purely determined by the hardware capabilities of the radio heliograph being significantly dependent on the image-restoration procedure.

For this reason, it was very difficult to carry out from two-dimensional SSRT images systematic studies of low-brightness features such as the center-to-limb brightness distribution, supergranulation network, filaments and prominences, coronal holes, etc. The first problem was due to the fact that the residual map below the final CLEAN level (threshold) is usually not processed but substituted with a model disk, so that all low-brightness features disappear. A satisfactory way to recover the residual map was not developed. On the other hand, usage of dirty maps requires a lot of manual work to select appropriate images and can only be done in exceptional cases. This way cannot be used systematically, e.g., to enhance the sensitivity by the averaging of several images.

To overcome these limitations and actualize the potential dynamic range of the SSRT, we have implemented a new imaging technique based on a multi-scale CLEAN (MS-CLEAN) algorithm described by Cornwell (2008) and adjusted to the SSRT data with a recovery of the residual map. This technique combines the MS-CLEAN routine with the directly-imaging capability of SSRT and

produces enhanced-quality clean images automatically. From these images, it has become possible to study low-brightness solar features.

The operating frequency of the SSRT (5.7 GHz) is three-times lower than the lowest one of NoRH (17 GHz) that results in considerably larger opacities of microwave sources observed by the SSRT with respect to 17 GHz ones to both the thermal free-free and gyromagnetic emissions. This circumstance determines a vast variety of contributions from chromospheric to coronal features in SSRT images.

Microwave observations of the quiet Sun at different frequencies have been reviewed by Kundu (1982) and more recently by Shibasaki et al. (2011). Microwave observations also offer wide opportunities to study active low-brightness features such as eruptive prominences and filaments from SSRT and NoRH images, as has been demonstrated by, e.g., Hanaoka et al. (1994b); Uralov et al. (2002); Shimojo et al. (2006); Grechnev et al. (2003; 2006a; 2006b) and others.

Among the issues, which can be addressed by the analysis of the enhanced-quality SSRT images, there are the following. The brightness distribution over the quiet Sun depends on the parameters of the solar atmosphere and is promising to elaborate the models. This distribution and its solar cycle variations at 17 GHz have been studied in detail from NoRH data (e.g., Nindos et al. 1999; Selhorst et al. 2004; 2011); however, only occasional measurements in longer microwaves have been known (e.g., Kundu 1982; Krissinel' 2005), whose results do not completely correspond to each other.

The microwave response to the supergranulation network has been first detected at 2–4 cm in one-dimensional observations with the RATAN-600 radio telescope (Bogod & Korolkov 1975; Bogod 1978). First two-dimensional microwave observations of the network with the Westerbork Synthesis Radio Telescope (WSRT) at a close (to SSRT) wavelength of 6 cm have been reported by Kundu et al. (1979). Comparison of the microwave observations

with the optical ones in the  $\text{Ca}^+$  K line has shown their correspondence. Benz et al. (1997) compared observations of the network with the Very Large Array (VLA) in microwaves at of 1.3, 2.0, and 3.6 cm with magnetic network elements and soft X-ray images produced by Yohkoh/SXT. The authors found the highest correspondence with magnetic network elements at the shortest wavelengths that decreased at 3.6 cm and was lowest in soft X-rays. There were very few similar observations with non-solar-dedicated WSRT and VLA telescopes, so that the data they provided are unique. The routine SSRT data appear to be promising to study the ‘microwave network’ as well.

In this paper we discuss the technique to routinely produce solar images at the SSRT and its elaboration. We present some beacon results on low-brightness features obtained in the analysis of enhanced-quality images to illustrate the opportunities of the SSRT. Elaboration of these results promises important contribution to the solar physics. We also compare the SSRT data with images produced by the Nobeyama Radioheliograph at 17 GHz as well as observations in different spectral ranges.

Section 2 outlines the imaging technique routinely used at the SSRT to deconvolve bright sources in active regions and describes our elaborated technique to produce the enhanced-quality images. Section 3 briefly describes the techniques to construct the microwave synoptic maps and to supplement the microwave images with the magnetic field data. Section 4 outlines observations of some low-brightness features. Section 5 presents a brief summary and outlines the long-standing problems and the plans.

## 2. SSRT Imaging Techniques

We consider the techniques to produce deconvolved images from ‘dirty’ SSRT data without an emphasis on the formation of the solar images with the SSRT. A description of the latter issue can be found in Smolkov et al. (1986) and Grechnev et al. (2003).

### 2.1. Imaging of Bright Sources in Active Regions

The SSRT produces images directly without measuring visibilities. The interactive CLEAN technique (Lesovoy 2002) routinely used for the SSRT data for more than one decade provides imaging of active regions in semi-automatic mode, consuming time and efforts. The corresponding viewable SSRT images as well as digital data in FITS format (one pair of single-pass images per day) are available at <http://www.ssrt.org.ru/> and <ftp://iszf.irk.ru/pub/ssrt>.

### 2.2. Advanced Imaging Technique

To achieve a fully automatic imaging at the SSRT with enhanced opportunities capable of reproducing low-brightness features, a hybrid approach was developed (Kochanov et al. 2011). The deconvolution is based on a multi-scale version of the CLEAN algorithm (Cornwell 2008). The MS-CLEAN has been adjusted for the SSRT

imaging and supplemented with an additional adaptive filtering to suppress residual noises and errors of the MS-CLEAN algorithm. The major feature of the new technique is processing of the residual map to recover low-brightness objects.

#### 2.2.1. Multi-Scale CLEAN for SSRT

We have found the MS-CLEAN algorithm to be most suitable to produce ‘clean’ images with the SSRT. While implementing the MS-CLEAN, selection of a proper size is crucial for each spatial scale. If the selected scale is too small, then false sources appear in a ‘clean’ map (‘fringing’ effect). If the selected scale is too large, then the source in the ‘clean’ map becomes excessively smoothed, and a spurious dark halo appears in the residual.

We have made several modifications of the original MS-CLEAN algorithm to adapt it to the SSRT imaging. Below we describe our algorithm using the notations according to Cornwell (2008) and omitting some details, which can be found in this paper.

- Initialize
  - Model Image:  $I^m = 0$
  - Residual image:  $I^R = \text{dirty image}$
  - For each scale  $\alpha$ 
    - Calculate the ‘clean’ beam  $m_c(\alpha) = H(r) \left[ 1 - \left(\frac{r}{\alpha}\right)^2 \right]$ , where  $r$  is the radial distance and  $H(r)$  is a Hanning window function of  $2\alpha$  width centered at  $r = 0$
    - Calculate the scale-convolved ‘dirty’ beam  $m(\alpha) = \text{PSF} * m_c(\alpha)$  (‘\*’ denotes convolution)
    - Calculate the scale-convolved residual as  $I_\alpha^R = I^R * m(\alpha)$ .
    - Calculate the scale normalization coefficient  $S(\alpha) = 1 / \sqrt{\sum_{x,y} m(\alpha)^2}$
    - For each pair of scales  $(\alpha_p, \alpha_q)$  calculate the cross term  $B * m(\alpha_p) * m(\alpha_q)$
- Repeat
  - Find the position of the maximum on the residual map  $I^R$  (modified)
  - Choose the scale with a maximum residual value at the selected position after multiplying by the scale-dependent normalization coefficient  $S(\alpha)$
  - Add this component scaled by the loop gain and convolved with the ‘clean’ beam of the selected scale to the current model.
  - Update all residual images using the pre-computed terms.
- Until
  - Either maximum iteration number reached
  - Or  $\max(I^r) < (\text{CLEAN threshold})$
- Finalize
  - add the residual  $I^R$  to the model  $I^m$  to get the restored image

To prevent selecting the largest scale in all iterations, the original MS-CLEAN algorithm uses the scale biases:

$$S(\alpha) = 1 - 0.6\alpha/\alpha_{\max} \quad (1)$$

Cornwell (2008) found this relations to work well with VLA images of radio galaxies. A disadvantage of this solution is that the scale bias (1) depends on the maximum scale  $\alpha_{\max}$ . This is the main reason why the original MS-CLEAN provides different results with different scale sets. Selecting an appropriate scale set is a tricky exercise, which is not possible to carry out in an automated image processing. Instead of the scale bias (1), we use a scale normalization coefficient:

$$S(\alpha) = 1/\sqrt{\sum_{x,y} m(\alpha)^2} \quad (2)$$

The usage of (2) makes the scale-convolved residuals proportional to the normalized convolution:

$$I_{\alpha}^R S(\alpha) = \frac{I^R * m(\alpha)}{\sqrt{\sum m(\alpha)^2}} \sim \frac{I^R * m(\alpha)}{\sqrt{\sum (I^R)^2 \sum m(\alpha)^2}} \quad (3)$$

Equation (3) has a maximum of 1.0 when the residual image  $I^R$  exactly matches the scale-convolved PSF,  $m(\alpha)$ ; otherwise, it is less than 1.0. By using this approach, the algorithm selects the scale with a scaled PSF,  $m(\alpha)$ , best matching the residual image.

Thus, oppositely to the original MS-CLEAN algorithm, our scheme adopted for SSRT data determines the position of the new clean component by searching the maximum of the unscaled residual image, but not by looking for the global maximum among all of the scale-convolved residuals. We do so to follow the ‘up-down’ scenario, i.e., to clean the image starting from bright sources and proceeding down to background features, which exceed the CLEAN threshold.

Due to properties of the SSRT construction, the PSF is not known with a required accuracy. Therefore, no modification of the CLEAN method is able to completely reconstruct SSRT images and to suppress all contributions from the beam’s side lobes. For this reason, a high CLEAN threshold is applied to avoid a large number of false sources in the ‘clean’ map. We have empirically found for the SSRT images the threshold of  $n\sigma_{\text{HF}}$ , where  $\sigma_{\text{HF}}$  characterizes high spatial-frequency fluctuations in a raw image, and  $n \approx 25$ . After the cleaning process, low-brightness features like filaments and coronal bright points remain on the residual map being partly distorted by the side lobes.

### 2.2.2. Recovery/Filtering of Residual Map

After the deconvolution process with the elaborated MS-CLEAN algorithm, an additional residual filtering is performed. The filtering should remove remaining contributions from the side lobes and preserve all quiet solar features.

At the first step, we find areas in the image, where remaining contributions from the side lobes are significant. To identify these areas, we calculate a parameter characterizing typical excursions along the directions of the

residual stripes due to the contribution from side lobes. This parameter is computed as a median value over the standard deviations in partial regions selected by a boxcar moving along the stripes. The areas, in which this parameter exceeds a pre-selected threshold, are considered to be contaminated by side lobes.

At the second step, an iterative procedure is performed, which removes the contributions from the side lobes by using non-distorted surrounding areas as a reference. This procedure operates in a CLEAN-like ‘up-down’ scenario. The CLEAN decomposes an image into a set of ‘clean components’ convolved with the PSF. Instead, our iterative filter decomposes an image into a set of overlapping image components, each of which is a smoothed sub-image multiplied by a Hanning window. The algorithm filters out those components, which are most likely contributions of side lobes, and reassemble the filtered image from the remaining ones. The scheme of this iterative procedure is as follows.

- Initialize
  - Residual image:  $I^R = \text{CLEAN residual}$
  - Filtered image:  $I^f = 0$
  - Filter width:  $\sigma_f$ .
  - Component width:  $\sigma_c$ .
  - Smooth width:  $\sigma_s$ .
  - High pass filtered image:  $I^{hp} = I^R - I^R * G(\sigma_f)$ , where  $G(\sigma_f)$  is a 2d Gaussian function with a width of  $\sigma_f$ .
- Repeat
  - Find the maximum of  $|I^{hp}|$
  - Extract from  $I^{hp}$  a sub-image  $I_s^{hp}$  as wide as  $\sigma_w$  centered at the position of the maximum.
  - Calculate the current image component  $C_i$  by multiplying the sub-image by Hanning window and convolving it with a Gaussian function  $C_i = (I_s^{hp} H) * G(\sigma_s)$ .
  - Subtract  $C_i$  from both  $I^R$  and  $I^{hp}$
  - Check if the  $C_i$  position lies inside the area, where the remaining contributions from the side lobes are significant. Otherwise, add  $C_i$  to the model image  $I^f$ .
  - Recalculate  $I^{hp}$  every 10 iterations.
- Until
  - Either maximum iteration number reached
  - Or  $\max(|I^r|) < \text{threshold}$
- Finalize
  - Add the remaining residual  $I^R$  to the filtered image  $I^f$  to get the result.

This algorithm has four important parameters. The filter width,  $\sigma_f$ , sets the width of the reference area surrounding every image component. This are should be, at least, 2–3 times wider than the major PSF lobe (the major maximum of the interference beam pattern). The component width,  $\sigma_c$ , sets the size of the sub-images used for

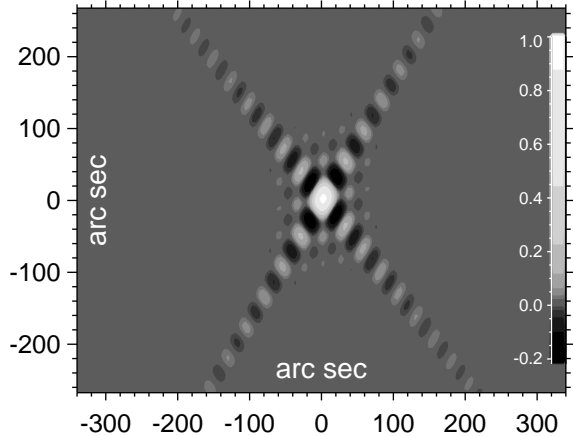


**Fig. 3.** The SSRT PSF used as an input for the deconvolution process. The observation time and field of view correspond to those in Figure 2c, d.

the decomposition. This width should slightly exceed the main PSF lobe. The smoothing width,  $\sigma_s$ , is a smoothing parameter used in the calculation of the components from the sub-images. This width should be considerably less than the major PSF lobe. The last parameter is the filter threshold. The standard deviation of the CLEAN residual is a good choice for this parameter.

Figure 2 presents an example of a dirty single-pass SSRT image observed on 2011 May 5 (a) and the result of its processing with deconvolution and filtering (b). The enlarged framed area containing active region sources is shown in the lower row (c, d). The beam model used in the CLEAN/filtering of this image is presented in Figure 3.

To assess both qualitatively and quantitatively how realistic the SSRT images after the CLEAN/filtering are, we compare them with NoRH 17 GHz data and extreme-ultraviolet images. To enhance the sensitivity of the SSRT images down to  $\lesssim 500$  K, we have averaged several tens of single-pass images observed on that day with a preparatory compensation for the solar rotation. The same averaging procedure has been done for 46 pairs of the NoRH snapshots produced in steps of 10 min.

We juxtapose in Figure 4 the daily-integrated microwave images of the Sun observed on 2011 May 5 by the SSRT at 5.7 GHz (a,b) and NoRH at 17 GHz (d,e) with SDO/AIA snapshots produced in the transition-region He II 304 Å line (c) and in the coronal Fe XII 193 Å line (f). The microwave images present the circular polarization (Figure 4a,d) and total intensity (Figure 4b,e). Besides bright coronal structures visible in the NoRH image, the enhanced-quality SSRT image clearly shows chromospheric structures. Prominences and filaments are also clearly visible.

The brightness temperature over the 17 GHz Stokes  $I$  image does not exceed 27 000 K. The strongest polarized emission of  $-366$  K occurs in the west negatively-polarized source, in which the degree of polarization does not exceed  $-20\%$ . All other sources are polarized up to  $\pm 5\%$ . Thus, the polarized emission at 17 GHz in this image is most

likely due to optically thin thermal bremsstrahlung.

The brightness temperatures in the major negatively polarized sources at 5.7 GHz reach in total intensity 0.6 MK in the East source and 0.9 MK in the West source. Both these sources have the degree of polarization of about 40%. These properties indicate a gyroresonance emission at 5.7 GHz. The dissimilarities between the SSRT and NoRH images observed at three-times different frequencies correspond to expectations; while the third-harmonic gyroresonance emission occurs at 5.7 GHz in a magnetic field of 680 G, even the fifth-harmonic emission at 17 GHz requires 1200 G at the base of the corona.

### 2.2.3. Calibration Technique

The SSRT images are calibrated in brightness temperatures as  $I = (RCP + LCP)/2$  and  $V = (RCP - LCP)/2$ , respectively, referring to the quiet Sun's brightness temperature  $T_{QS} = 16\,000$  K (Zirin et al. 1991; Borovik 1994). Initially, the technique used to calibrate NoRH images (Hanaoka et al. 1994a) was adopted at the SSRT. This calibration technique is based on the analysis of the brightness distribution in an image, in which two statistical peaks should be present. One of them corresponds to the zero sky level, and the second one corresponds to the quiet Sun's level. The images are calibrated by referring to the positions of the maximum values in the two peaks.

Later we have elaborated this technique to improve its stability and accuracy. They are especially critical for the SSRT images because of their lower quality relative to NoRH ones, intrinsically broader quiet Sun's brightness distribution at 5.7 GHz due to the larger contribution from inhomogeneities in the chromosphere and corona, including the higher limb brightening as discussed in section 4. At the present time, we analyze the brightness distribution within the solar disk and outside it separately, as Figure 5 illustrates.

Two columns in the figure present two single-pass SSRT images observed with an interval of 12 min but formed in somewhat different conditions. The portions of the dark disks in the upper left and lower right corners of Figure 5a are due to the negative response from the adjacent interference numbers. The blank gray triangle area in the upper left corner of Figure 5d is due to missing data. The middle panels show the histograms computed over the whole images. The lower panels show the gray histograms computed separately for the quiet-Sun area inside the dotted circle shown in the upper panels and the sky area computed outside the dashed circle. Each of the peaks of separate histograms shown in the lower panels is fitted with a Gaussian (black curves), and their calculated positions are used to calibrate the images.

The position of the quiet Sun's level is displaced with respect to the apparent maximum of the right peak in Figure 5b, while the two peaks in the histogram in Figure 5e is difficult to recognize. These examples illustrate the robustness of the advanced technique.

This calibration technique has turned out to be useful for NoRH images also. Their calibration stability becomes problematic, when the brightness temperatures of sources of interest are comparable with the clean threshold. Our

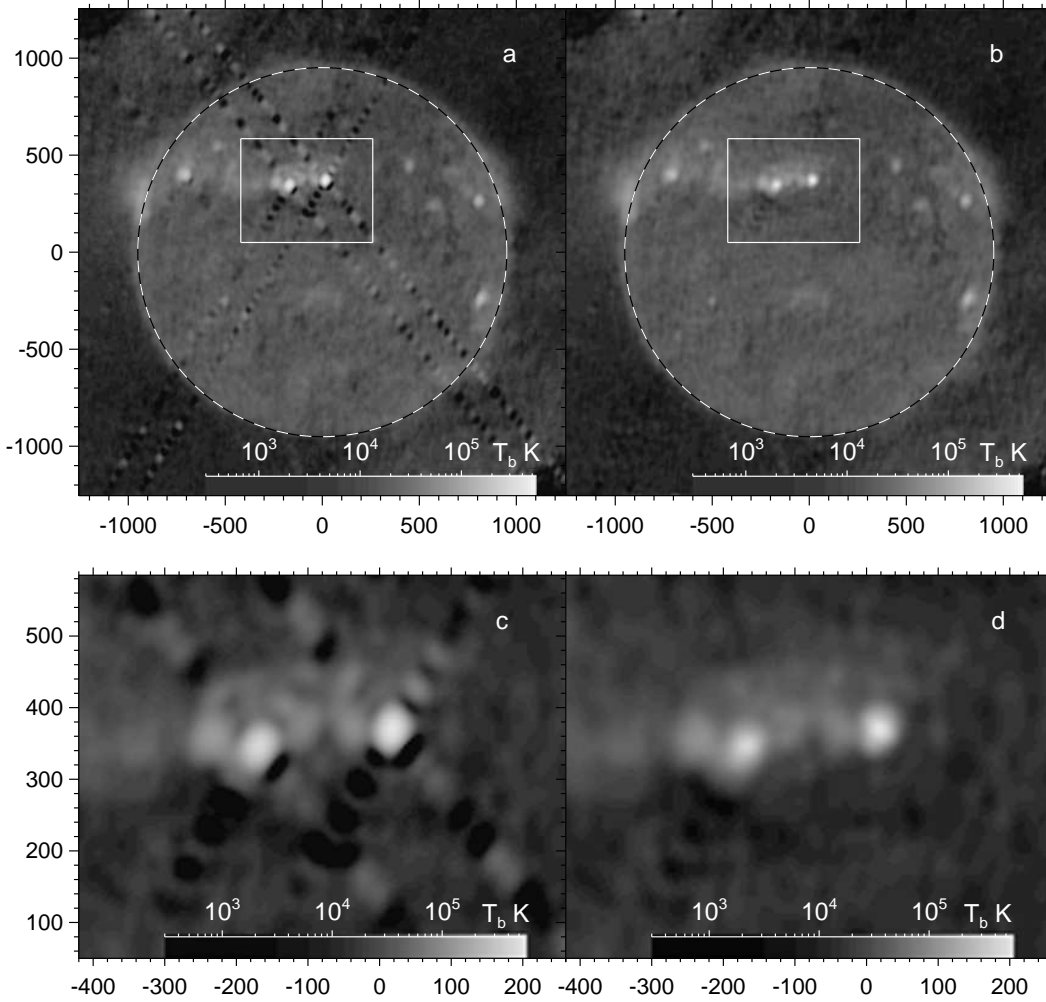


**Fig. 2.** Single SSRT images observed on 2011 May 5: dirty image (a) and clean image (b). The lower panels show the enlarged parts of the dirty (c) and clean (d) images marked by the white frame in the panels above them. The axes show hereafter in similar images the distances from the solar disk center in arc seconds. The gray scale bars quantify the images in brightness temperatures.

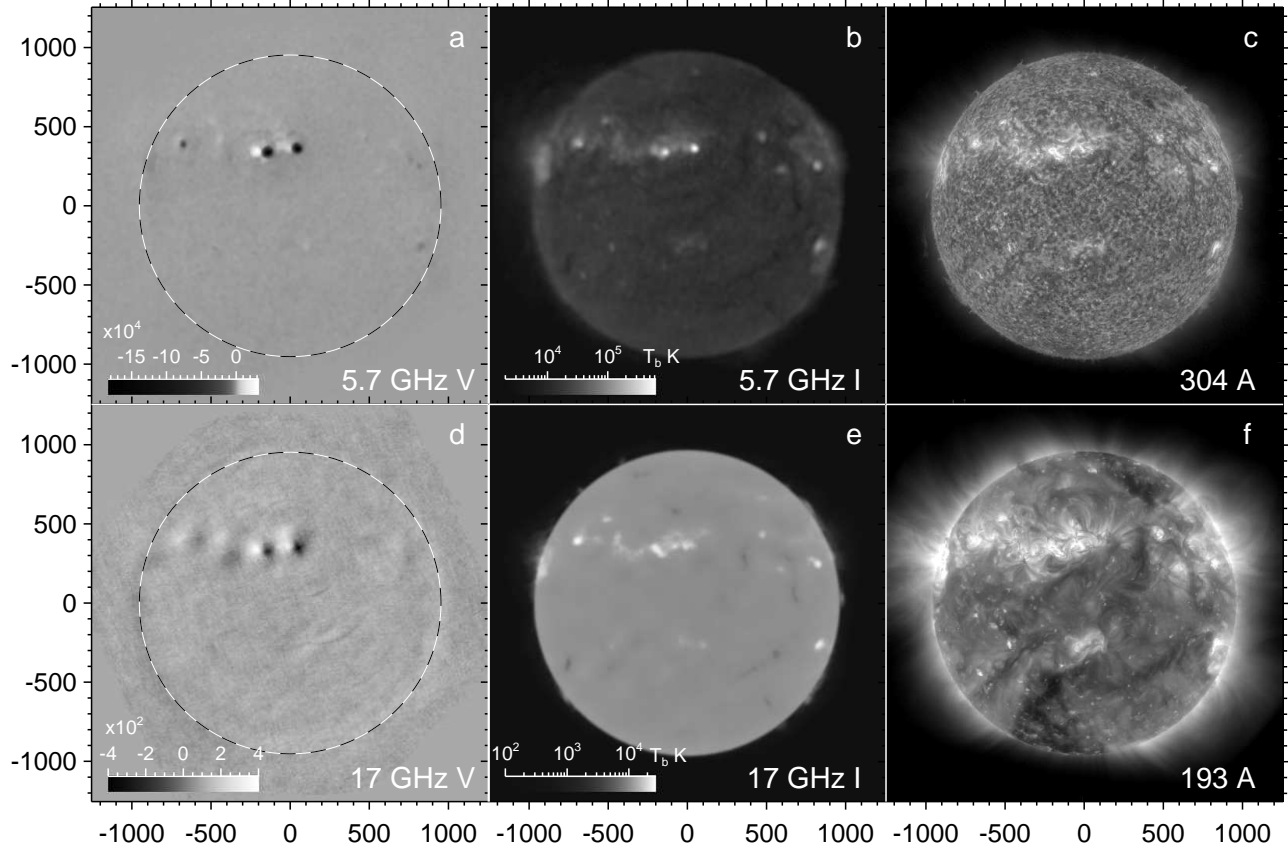
elaborated technique allows us to improve the calibration quality of NoRH images considerably.

Figure 6 illustrates the result of recalibration of the NoRH images produced during a very weak burst caused by a non-active-region filament eruption on 2011 May 11. The histogram for the quiet Sun was computed within the dotted circle, and the histogram for the sky was computed within the wide ring between the dashed circles. The gray time profile in Figure 6b was computed over the burst source area inside the solid contour from a set of images with 10 s integration time produced by the Koshix program in steps of 10 s. The black time profile was computed from recalibrated images. The total flux of the Sun at 17 GHz on that day was 630 sfu. Figure 6c compares the time profiles of the burst recorded with NoRH at 17 GHz and SSRT at 5.7 GHz. Their close correspondence to each other certifies almost purely thermal nature of the microwave burst. On the other hand, this example demonstrates that measurements from NoRH data can be still improved.

The elaborated techniques described in the present Section 2 have automatically produced enhanced-quality SSRT images for many days of observations. Several observational intervals still remain, for which attempts to produce such images were not successful; routine SSRT data can be used for these days. The new data set processed to the present time offers wide opportunities to study low-brightness features at 5.7 GHz. Some examples are considered in section 4. The data base of enhanced-quality daily averaged SSRT images is regularly updated and available at <http://ssw.iszf.irk.ru>.

### 3. Computation of Synoptic Maps from SSRT Images

Daily radio brightness distributions of total intensity and polarized emission accumulated in our data base supplemented with synoptic distributions for the Carrington rotations of the Sun. In computation of a required rotation we use a set of full-disk daily images, which correspond to a time interval starting from the middle of the



**Fig. 4.** Comparison of solar images produced on 2011 May 5 in different spectral ranges. Top row: SSRT 5.7 GHz (a, polarized emission; b, total intensity) and SDO/AIA 304 Å (c). Bottom row: NoRH 17 GHz (d, polarized emission; e, total intensity) and SDO/AIA 193 Å (f). All the SSRT and NoRH images shown here are daily averages; the SDO/AIA images are snapshots. The dashed circles in panels (a) and (d) denote the optical limb.

preceding rotation and ending at the middle of the next one. In the computation of such a map, we use a synoptic grid of  $[1080 \times 540]$  samples on the surface of the Carrington longitude and the sine of the latitude within the intervals of  $[1/6, 360 - 1/6]$  and  $[-1 + 1/540, 1 - 1/540]$ , respectively. Each node  $(l, j)$  of the grid is associated with a Julian day  $JD_{\text{net}}^{\text{SYN}}$  corresponding to the Carrington longitude of the node. To calculate the necessary synoptic quantity in a selected node  $(l, j)$  of the synoptic map, the following operations are carried out:

1. From each full-disk data array, a value is interpolated to each current node of the synoptic grid, if this node belongs to the current plane of the sky. As a result, two one-dimensional arrays are formed. One array contains interpolated values  $f$ , and another array contains Julian dates  $JD$  corresponding to the observation times of the full-disk images, from which the values to be interpolated were selected. Both one-dimensional arrays have the same number of elements  $M$ , and the index  $s = 1, 2, \dots, M$ . Generally,  $M < N$ , where  $N$  is the total number of the full-disk source images, and  $M$  depends on the position of the node  $(l, j)$ .
2. The ultimate value of a synoptic parameter for a

node  $(l, j)$  is calculated as a weighted average:

$$F^{\text{SYN}}(i, j) = \frac{\sum_{s=1}^M f(s) a(s)}{\sum_{s=1}^M a(s)}, \quad (4)$$

where  $a(s) = \exp\left\{-\left[12.9 \frac{JD_{\text{net}}^{\text{SYN}}(i, j) - JD(s)}{27.275}\right]^2\right\}$ ; 12.9 is a weighting factor optimized experimentally.

Equation (4) provides the largest contribution from those pixels in a full-disk image, whose distance is minimum from the central meridian corresponding to the Carrington longitude of the node  $(l, j)$ . The calculated synoptic data for each Carrington rotation are recorded into FITS files and posted to the main data base.

All microwave images are combined with a corresponding potential magnetic field. The graphic files are produced for both daily full-disk images and synoptic maps and posted to the same data base. The magnetic field is calculated from the coefficients of the spherical harmonic decomposition contained in the BD-Monitoring data base (<http://bdm.iszf.irk.ru/>).

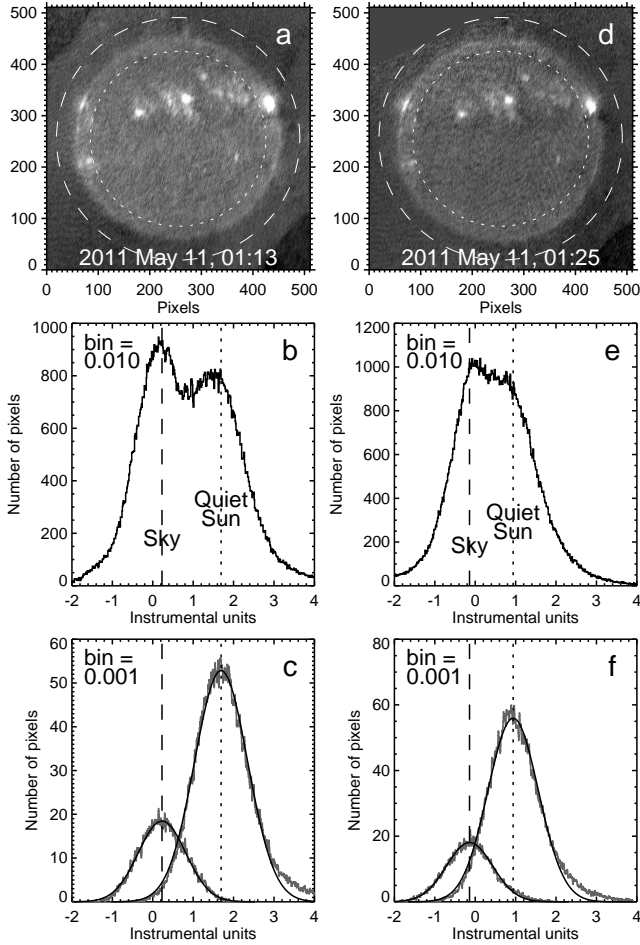


**Fig. 5.** Calibration of SSRT images illustrated with two examples shown in the left and right columns. a), b): raw images to be calibrated. The histograms are calculated separately within the area limited by the dotted circle (quiet Sun) and outside the dashed circle (sky). b), e): the histograms calculated over the whole images. c), f): the histograms calculated for the sky and quiet Sun separately (gray) along with the Gaussian fit (black).

#### 4. Low-brightness Features in SSRT Images

Microwave observations of the quiet Sun have been reviewed by Kundu (1982) and more recently by Shibasaki et al. (2011). Active low-brightness features such as eruptive prominences and filaments in microwave SSRT and NoRH images have been also discussed previously (e.g., Hanaoka et al. 1994b; Uralov et al. 2002; Shimojo et al. 2006; Grechnev et al. 2003; 2006a; 2006b; and others). Here we briefly present low-brightness features in enhanced-quality SSRT images, which can contribute to further investigations into these issues.

##### 4.1. Brightness Temperature Radial Distribution

The average brightness temperature distribution was measured from 296 images produced by the SSRT from 2010 April 1 to 2010 September 30 and from 2011 April 1 to 2011 July 30. Before the measurements, daily averaged

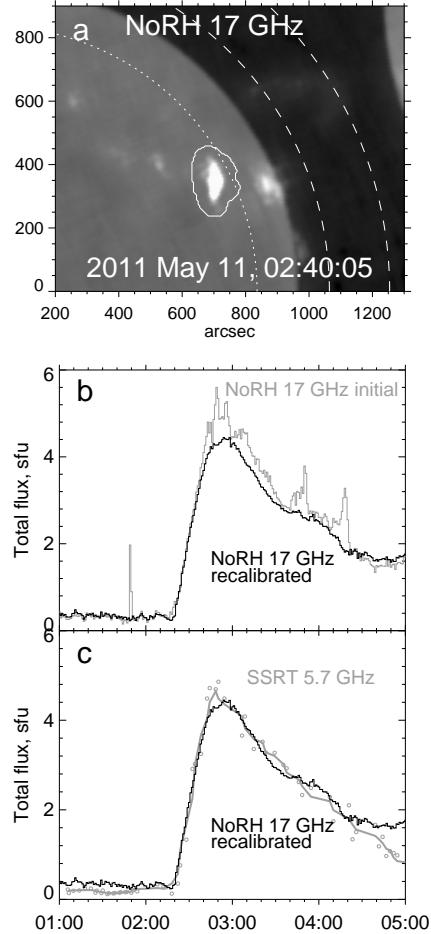


**Fig. 6.** Recalibration of NoRH 17 GHz data with the technique presented in Figure 5. a) A portion of a NoRH image with the contoured area of the thermal microwave source. The histograms were calculated separately within the dotted circle (quiet Sun) and within the wide ring limited by the dashed circles (sky). b) Total flux time profiles computed within the contour from the initial NoRH images (gray) and after recalibration (black). c) Comparison of the total flux time profiles computed from NoRH images (black) and SSRT images (gray circles; solid gray curve is smoothed over 5 points).

SSRT images were additionally averaged over eight days. Then the averaged images were analyzed with ring scanning. The ring had a width of one pixel and progressively increasing radius. Data within each ring were analyzed statistically. All pixels with values deviating from an average value by more than  $\pm 2\sigma$  were discarded, and a new average calculated over remaining pixels was assigned as a brightness temperature at the current radius. This technique does not take account of the elliptical shape of the radio brightness distribution, and the result depends on the current situation on the Sun. The result is shown in Figure 7a. This is the first attempt to measure this distribution from two-dimensional SSRT images and can be elaborated in future.

For comparison we also computed the average brightness temperature distribution from NoRH 17 GHz snap-



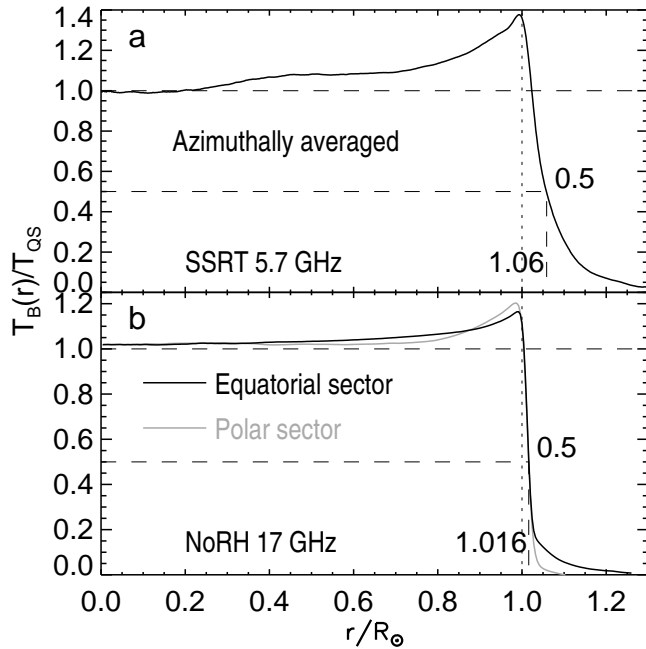


**Fig. 7.** Averaged radial distribution of the brightness temperature: a) SSRT, 5.7 GHz, azimuthally averaged distribution; b) NoRH, 17 GHz, in the equatorial (black) and polar (gray) sectors of  $15^\circ$  widths.

shots (one per day). Measurements from NoRH data covered the periods from 1992 July to 1995 August and from 1995 November to 1996 April (totally 44 months, about 1320 images). We carried out the measurements from monthly averaged NoRH images. In this case, the higher data quality and uniformity allowed us to analyze the brightness temperature distribution with a more complex algorithm in 24 sectors separately, each of  $15^\circ$ . The results are shown in Figure 7b.

The central part of the distribution at 5.7 GHz corresponds to the ‘bald’ Sun, while at  $r > 0.2R_\odot$  the brightness temperature increases by about 8% probably due to the contribution from active regions at mid latitudes. This contribution is present up to the limb because of the azimuthal averaging. The position of the inflection probably depends on the phase of the solar activity. The radio radius at a 0.5 level of the brightness at the disk center is about  $\approx 1.06R_\odot$ . The limb brightening spike reaches  $1.38T_{QS\ 5.7} \approx 22000$  K. These parameters are close to the measurements by Kundu et al. (1979) with WSRT at 6 cm that gave the radio radius of  $\approx 1.05R_\odot$  and the limb brightening up to 1.4–1.5 of the brightness temperature near the solar disk center. Our results are also mostly close to those measured by Krissinel’ (2005) from one-dimensional SSRT scans observed in the solar minimum. Unlike the results obtained from the one-dimensional SSRT data, a considerable polar limb brightening seems to be clearly present in most two-dimensional SSRT images, in accordance with the measurements at 6 cm reported by Kundu et al. (1979). This difference might be due to the solar cycle variations found by Selhorst et

al. (2004; 2011) for the quiet Sun at 17 GHz.

Our measurements show that the radio radius at 17 GHz amounts to  $1.016R_\odot$  (Figure 7b). The limb spike reaches  $1.16T_{QS\ 17}$  in the equatorial sector and  $1.20T_{QS\ 17}$  in the polar sector ( $T_{QS\ 17} = 10000$  K). These parameters of the limb brightening are consistent with those shown by Nindos et al. (1999) and the statistical results of Selhorst et al. (2004; 2011). All of these quantities were measured directly from SSRT and NoRH images without any correction for deconvolution.

#### 4.2. Supergranulation Network

It is possible to study the network in microwaves from SSRT images, although with a poorer spatial resolution of order  $25''$ . The relative stability of the network on the time scale of several hours allows one to use daily averaged SSRT images to improve the sensitivity. Figure 8 presents a comparison of the network appearance in the SSRT image averaged over 5 hours on 2010 July 7 along with the snapshots produced at about 05:00 by SDO/AIA in  $304\ \text{\AA}$ ,  $1600\ \text{\AA}$ , and the SDO/HMI magnetogram. We have additionally considered an averaged NoRH 17 GHz image and an SDO/AIA  $171\ \text{\AA}$  snapshot. We do not show them for the lack of any manifestations of the network in these images.

The upper row of Figure 8 shows the SSRT Stokes  $V$  image (a), raw SDO/AIA  $304\ \text{\AA}$  (b) and  $1600\ \text{\AA}$  (c) images, and the line-of-sight SDO/HMI magnetogram ( $B_{LOS}$ , d). To reveal weak polarized emission in the SSRT image, we have smoothed it with a boxcar of  $7 \times 7$  pixels size and limited the brightness from above by 1100 K. Actually source 1 reaches 3000 K, source 2 reaches 15400 K. The signs of the polarization of sources 1 and 2 are reverted and correspond to the o-mode emission, which is a well-known effect typically observed at low microwaves close to the limb. An extended plage region 3 with brightness temperatures exceeding  $\pm 1000$  K and a compact source 4 ( $-1500$  K) are polarized in the sense of the x-mode emission being located far from the limb.

All the images in the middle row, Figure 8e–h, are presented in the form corresponding to the SSRT resolution. These are the SSRT Stokes  $I$  image (e), SDO/AIA  $304\ \text{\AA}$  (f) and  $1600\ \text{\AA}$  (g) images smoothed by convolving with the SSRT beam pattern, and the absolute value of the line-of-sight SDO/HMI magnetogram ( $|B_{LOS}|$ , h).

The images in the lower row, Figure 8i–l, are enlarged portions of the images just above denoted by the frames: Stokes  $I$  at 5.7 GHz (i), SDO/AIA  $304\ \text{\AA}$  (j),  $1600\ \text{\AA}$  (k), and  $|B_{LOS}|$  (l). The contours on top of all of the images are the same and correspond to the levels of 4.5 G (white) and 6.8 G (black) in the smoothed  $|B_{LOS}|$  magnetogram. These contours facilitate visual comparison of the images with the  $|B_{LOS}|$  magnetogram.

The SSRT Stokes  $I$  image presents a range of brightness temperatures from 11000 K to 18500 K. Comparison of dark and bright features within the contours in the SSRT image with other images shows a good correspondence between some features (e.g., in the upper left corner) and a poor correspondence for some others (e.g., the

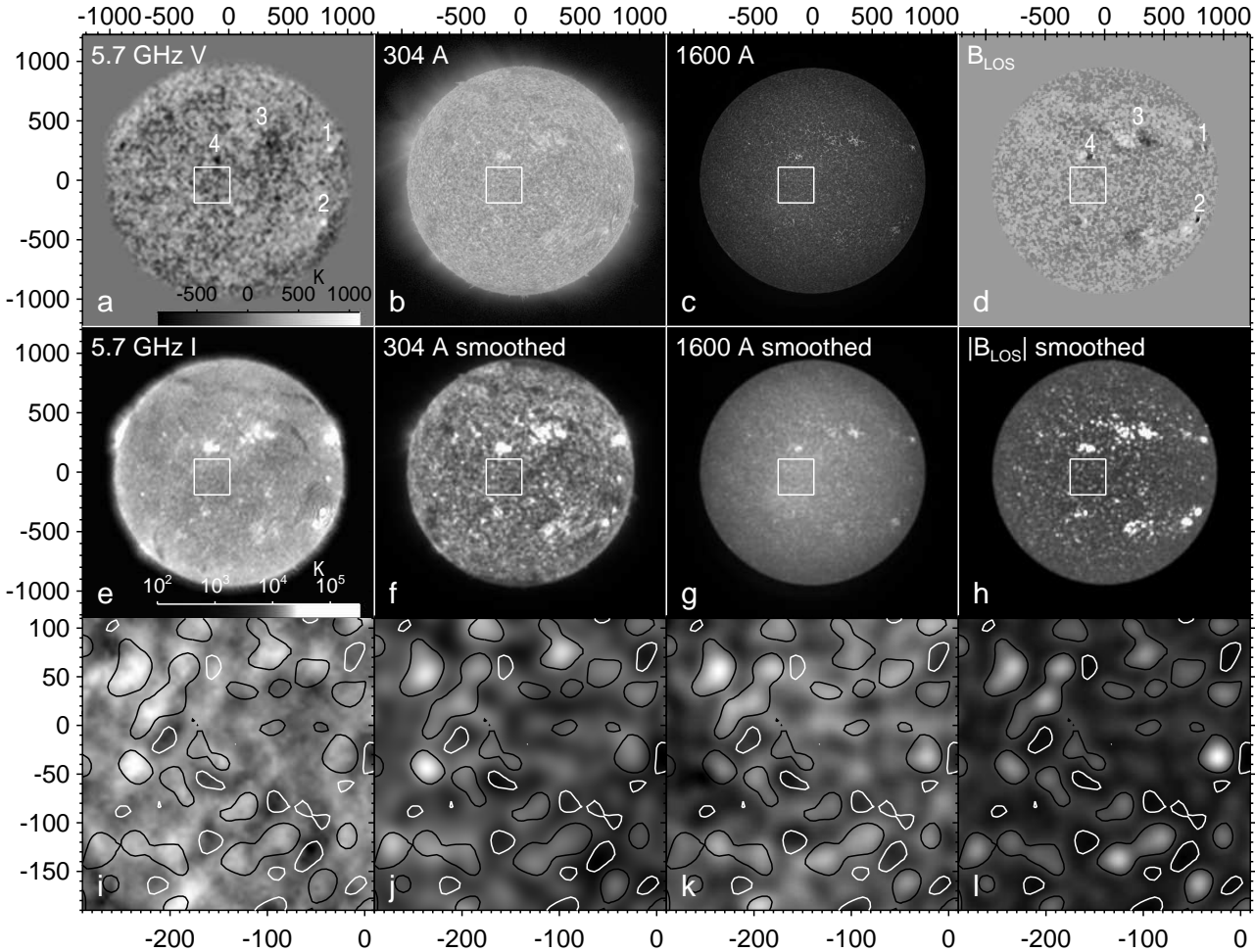


**Fig. 8.** Supergranulation network in microwave and EUV images (SDO/AIA) and the magnetogram (SDO/HMI) observed on 2010 July 7 (all displayed strongly nonlinearly). All the images in each column present the same wavelength. The images in the middle row present the images from the upper row with a spatial resolution reduced to the SSRT one. The lower row shows an enlarged area of the images in the middle row denoted by the white frame. The contours overlaid on all the images in the lower row correspond to the levels of 4.5 and 6.8 G in the smoothed  $|B_{\text{LOS}}|$  magnetogram.

brightest feature in the right middle part of the magnetogram). Nevertheless, an overall structural correspondence appears to be present. A careful examination can reveal extra matching features, which are not outlined with the contours. A typical brightness temperature of dark network elements at 5.7 GHz is about 12500 K, while that of bright elements is about 18000 K. Thus, the SSRT image shows a contrast of the network of about 1.44:1. This is somewhat less than the contrast estimated by Kundu et al. (1979) at 6 cm (1.7:1); the difference can be due to a  $\sim 30\%$  larger opacity to the free-free emission at 6 cm (WSRT) with respect to 5.2 cm (SSRT) as well as our usage of direct measurements without any correction for deconvolution. The cell sizes correspond to those observed by Kundu et al. (1979) at 6 cm,  $\sim (40 - 50)''$ .

To assess the correspondence between the SSRT and SDO/AIA images quantitatively, we have calculated the Pearson correlation coefficients for pairs of the images within the quite Sun area at the solar disk centre. The cal-

culcation was done for 10 image samples obtained at June–July 2010. The EUV images and  $|B_{\text{LOS}}|$  magnetograms were smoothed and resized to match spatial resolution of the SSRT. The results are summarised in Table 1.

The low correlation for the 171 Å coronal channel is expected: while the magnetic field is stronger at the footpoints of coronal loops, their brightness is maximum between the footpoints, as Benz et al. (1997) proposed. A noticeable coronal contribution at 5.7 GHz can be also responsible for the decreased correlation of the network shown by the SSRT with the magnetogram. The Pearson correlation coefficient between the SSRT image and the 304 Å image is the largest one, 0.68, and considerably less between the SSRT image and the 171 Å image, 0.5, but still higher than between the 171 Å image and the magnetogram. Note that bright coronal features look generally similar at 5.7 GHz and in 171 Å as well as 195 Å images (Grechnev et al. 2003; 2006a).

These facts confirm that SSRT images at 5.7 GHz show

	SSRT	HMI	AIA 1600 Å	AIA 304 Å	AIA 171Å
SSRT	—	$0.59 \pm 0.07$	$0.47 \pm 0.05$	$0.68 \pm 0.08$	$0.50 \pm 0.15$
HMI	$0.59 \pm 0.07$	—	$0.61 \pm 0.05$	$0.73 \pm 0.03$	$0.42 \pm 0.10$

**Table 1.** Pearson correlation coefficients for SSRT, SDO/AIA images, and SDO/HMI magnetograms.

a superposition of chromospheric and coronal contributions supplemented with compact gyromagnetic sources. Note also that the difference between the bright and dark network elements in SSRT images of 5500 K is well above the SSRT sensitivity (1500 K in a single image), which allows one to analyze the network manifestations on considerably shorter time scales than 5 hours used here.

We also analyzed a NoRH 17 GHz image averaged over the whole day of observations, but the supergranulation network was not detectable in this image for an obvious reason. The opacity of microwave sources at 17 GHz is less than at 5.7 GHz by about one order of magnitude, so that the range of brightness temperatures of 8000 K in the SSRT image in Figure 8i is expected to be at 17 GHz well below the CLEAN threshold (3000 K; it cannot be reduced considerably).

Finally we note that the quite Sun’s features discussed in this section determine an intrinsically wider histogram of the brightness temperature distribution at 5.7 GHz with respect to 17 GHz. The FWHM width of the histogram computed for the small region in Figure 8i is about 2500 K. The center-to-limb brightness temperature variation still increases the width. These circumstances offer additional requirements to the calibration technique at 5.7 GHz, as mentioned in section 2.2.3.

The beacon results presented here promise a considerably larger scientific outcome of the observations made with the SSRT. Elaboration of these results can contribute to further investigations into important issues of the solar physics.

## 5. Summary and Concluding Remarks

Several dozens of single-pass solar images have been produced by the SSRT every day. The elaborated techniques presented here have allowed us to deconvolve the images with restoration of low-brightness features in a fully automatic regime. Visual and quantitative comparisons with data from different spectral ranges and with the reported results previous studies at close wavelengths confirm reliability and high quality of the data produced with our new techniques. So far, the state-of-art does not allow us to produce high-quality data from all of the single-pass images. We hope to overcome this limitation.

A non-interrupted sequence is available of one single-pass SSRT image per day observed from 2000 May up to the most recent day. These images are produced with the routine SSRT CLEAN technique, which provides images of active regions, but does not reveal low-brightness features below the CLEAN threshold.

The daily averaged images with the enhanced dynamic range of  $\sim 30$  dB and brightness sensitivity  $\lesssim 500$  K have been produced for more than 80 months of SSRT observa-

tions from 1999 August to 2013 February (years 2007 and 2008 have not yet been successfully processed). These images allow one to study quasi-stationary solar features at 5.7 GHz such as the radial brightness temperature distribution, supergranulation network, coronal holes, bright points, filaments and prominences, and others. These data are easily accessible via the Internet.

The enhanced-quality single-pass SSRT images are also promising for studies of eruptive prominences and filaments. Depending on a particular situation, they can be observed in SSRT images up to distances exceeding  $2R_{\odot}$  from the solar disk center, i.e., with an overlap with the LASCO/C2 field of view. The list of eruptive prominences and filaments observed with the SSRT contains 89 events. Very few of these events have been analyzed so far.

The initial operating principle of the SSRT (see Section 1) has allowed us to produce images of rather high quality, but restricted the opportunities in the following aspects. The single-frequency capability of the SSRT is the first limitation. Second, due to the direct imaging, the receiver system is facing the whole dynamic range of the brightness temperatures that can considerably exceed  $10^3$  during flares. For this reason, it is very difficult to observe flares with the SSRT. And, third, each image of the Sun was produced by using the Earth’s rotation taking 3–5 min, so that the snapshot mode was impossible. An obvious way to overcome the second and third limitations is the change of the operating principle to the parallel synthesis. The implementation of the multi-frequency capability has also been developed.

In 2013 July the SSRT has terminated observations based on the initial operating principle. The SSRT is currently under the upgrade to a multi-frequency (4–8 GHz) radio heliograph. The new-generation solar radio telescope would consist of 96 antennas and occupy the East–West–South sub-array of the SSRT. A 10-antenna prototype of the radio heliograph was developed (Lesovoi et al. 2012). The following design questions have been resolved with the prototype: a suitable dual polarization feed; transmission of RF signal from the antennas to a working building; and, finally, interconnection of digital receivers and the correlator. The expected brightness temperature sensitivity of the radio heliograph is about 100 K in the snapshot image. The expected spatial resolution would be up to  $13''$ . The accuracy in the measurements of the degree of polarization is assumed to be up to a few percents.

**Acknowledgements.** We thank S. V. Lesovoi, A. M. Uralov, A. T. Altyntsev, B. B. Krissinel, K. Shibasaki, C. E. Alissandrakis, and S. M. White for fruitful discussions and assistance. We are indebted to the referee, Prof. Kameno, for useful remarks and

encouraging suggestions. We thank colleagues from Nobeyama Solar Radio Observatory (NAOJ) operating NoRH and NoRP, and colleagues operating the Siberian Solar Radio Telescope. We are grateful to the SDO/AIA and SDO/HMI consortia for their open data policy.

This study was supported by the Russian Foundation of Basic Research under grants 12-02-00037, 12-02-33110-mol-a-ved, 12-02-31746-mol-a, and 13-02-90472-ukr-f-a; the Program of base fundamental research of the SB RAS No. 16.1, and the Russian Ministry of Education under projects 8407 and 14.518.11.7047.

## References

- Alissandrakis, C. E., Lubyshev, B. I., Smol'kov, G. I., et al. 1992, *Sol. Phys.*, 142, 341
- Altynsev, A. T., Grechnev, V. V., Kachev, L. E., Lesovoi, S. V., Mansyrev, M. I., Molodyakov, S. A., Platonov, A. V., Saenko, I. I., Smolkov, G. Y., Sych, R. A., Treskov, T. A., Zandanov, V. G., Esepkina, N. A. 1994, *A&A*, 287, 256
- Benz, A. O., Krucker, S., Acton, L. W., Bastian T. S. 1997, *A&A*, 320, 993
- Borovik, V. N. 1994, *Lecture Notes in Physics, Advances in Solar Physics*. Catania, Italy, 11–15 May, 1993, 432, 185
- Bogod, V. M., & Korolkov, D. V. 1975, *Pisma v Astronomicheskii Zhurnal*, 1, 25
- Bogod, V. M. 1978, *Soobshcheniya Spetsial'noj Astrofizicheskoy Observatorii*, 23, 22
- Cornwell, T. J. 2008, *IEEE Journal of Selected Topics in Signal Processing*, 2, 793
- Enome, S. 1995, *Coronal Magnetic Energy Releases*, 444, 35
- Grechnev, V. V., Lesovoi, S. V., Smolkov, G. Y., Krissinel, B. B., Zandanov, V. G., Altynsev, A. T., Kardapolova, N. N., Sergeev, R. Y., Uralov, A. M., Maksimov, V. P., Lubyshev, B. I. 2003, *Sol. Phys.*, 216, 239
- Grechnev, V. V., Uralov, A. M., Maksimov, V. P., Zandanov, V. G., Smolkov, G. Y., Altynsev, A. T., Krissinel, B. B., Kardapolova, N. N., Lesovoi, A. V., Lubyshev, B. I., Prosovetsky, D. V., Rudenko, G. V.: 2006a, *Solar Physics with the Nobeyama Radioheliograph*, 101
- Grechnev, V. V., Uralov, A. M., Zandanov, V. G., Baranov, N. Y., Shibasaki, K. 2006b, *PASJ*, 58, 69
- Hanaoka, Y., Shibasaki, K., Nishio, M., Enome, S., Nakajima, H., Takano, T., Torii, C., Sekiguchi, H., Bushimata, T., Kawashima, S., Shinohara, N., Irimajiri, Y., Koshiishi, H., Kosugi, T., Shiomi, Y., Sawa, M., Kai, K. 1994a, *Proceedings of Kofu Symposium*, 35
- Hanaoka, Y., Kurokawa, H., Enome, S., Nakajima, H., Shibasaki, K., Nishio, M., Takano, T., Torii, C., Sekiguchi, H., Kawashima, S., Bushimata, T., Shinohara, N., Irimajiri, Y., Koshiishi, H., Shiomi, Y., Nakai, Y., Funakoshi, Y., Kitai, R., Ishiura, K., Kimura, G. 1994b, *PASJ*, 46, 205
- Högbom, J. A. 1974, *A&AS*, 15, 417
- Kochanov, A. A., Anfinogentov, S. A., Prosovetsky D. V. in *Solar and Solar-Terrestrial Physics 2011*, Proc. 16-th Pulkovo International Conference on Solar Physics (GAO RAN, St. Petersburg, Pulkovo, 2011), 227
- Koshiishi, H., Enome, S., Nakajima, H., et al. 1994, *PASJ*, 46, L3
- Krissinel, B. B. 2005, *Astron. Rep.*, 49, 939
- Krissinel, B. B., Kuznetsova, S. M., Maksimov, V. P., Prosovetsky, D. V., Grechnev, V. V., Stepanov, A. P., Shishko, L. F. 2000, *PASJ*, 52, 909
- Kundu, M. R. 1982, *Reports on Progress in Physics*, 45, 1435
- Kundu, M. R., Rao, A. P., Erskine, F. T., Bregman, J. D. 1979, *ApJ*, 234, 1122
- Lesovoy, S. V. 2002, *Radiophysics and Quantum Electronics*, 45, 865
- Lesovoi, S. V., Altynsev, A. T., Ivanov, E. F., Gubin, A.V. 2012, *Sol. Phys.*, 280, 651
- Maksimov, V. P., Prosovetsky, D. V., Grechnev, V. V., Krissinel, B. B., Shibasaki, K. 2006, *PASJ*, 58, 1
- Nakajima, H., Nishio, M., Enome, S., Shibasaki, K., Takano, T., Hanaoka, Y., Torii, C., Sekiguchi, H. et al. 1994, *Proc. IEEE*, 82, 705
- Nakajima, H., Sekiguchi, H., Sawa, M., Kai, K., Kawashima, S. 1985, *PASJ*, 37, 163
- Nindos, A., Kundu, M. R., White, S. M., Gary, D. E., Shibasaki, K., Dere, K. P. 1999: *ApJ*, 527, 415
- Rudenko, G. V. 2001, *Solar Phys.*, 198, 5
- Selhorst, C. L., Silva, A. V. R., Costa, J. E. R. 2004, *A&A*, 420, 1117
- Selhorst, C. L., Giménez de Castro, C. G., Válio, A., Costa, J. E. R., Shibasaki, K. 2011, *ApJ*, 734, 64
- Shibasaki, K., Alissandrakis, C. E., Pohjolainen, S. 2011, *Sol. Phys.*, 273, 309
- Shimojo, M., Yokoyama, T., Asai, A., Nakajima, H., Shibasaki, K. 2006, *PASJ*, 58, 85
- Smolkov, G. I., Pistolkors, A. A., Treskov, T. A., Krissinel, B. B., Putilov, V. A. 1986, *Ap&SS*, 119, 1
- Steer, D. G., Dewdney, P. E., Ito, M. R. 1984, *A&A*, 137, 159
- Uralov, A. M., Grechnev, V. V., Lesovoi, S. V., Sych, R. A., Kardapolova, N. N., Smolkov, G. Ya., Treskov, T. A. 1998, *Sol. Phys.*, 178, 557
- Uralov, A. M., Lesovoi, S. V., Zandanov, V. G., Grechnev, V. V. 2002, *Sol. Phys.*, 208, 69
- Uralov, A. M., Grechnev, V. V., Rudenko, G. V., Rudenko, I. G., Nakajima, H. 2008, *Sol. Phys.*, 249, 315
- Zirin, H., Baumert, B. M., Hurford, G. J. 1991, *ApJ*, 370, 779